Ocean Engineering 66 (2013) 92–100

Contents lists available at SciVerse ScienceDirect

Ocean Engineering

journal homepage: www.elsevier.com/locate/oceaneng

# Modelling and simulation of the sea-landing of aerial vehicles using the Particle Finite Element Method

P. Ryzhakov [a,*], R. Rossi [a], A. Viña [b], E. Oñate [a]

[a] Centre Internacional de Mètodes Numèrics en Enginyeria (CIMNE), Spain
[b] CIMSA Ingenieria de Sistemas, Spain

ARTICLE INFO

*Article history:*
Received 22 October 2012
Accepted 30 March 2013
Available online 10 May 2013

*Keywords:*
Fluid–structure interaction
Water landing
UAV
PFEM
Wedge impact
Incompressible flows

ABSTRACT

In this paper the Particle Finite Element Method (PFEM) is applied to the simulation of the sea-landing of an unmanned aerial vehicle (UAV). The problem of interest consists in modelling the impact of the vehicle against the water surface, analyzing the main kinematic and dynamic quantities (such as loads exerted upon the capsule at the moment of the impact). The PFEM, a methodology well-suited for free-surface flow simulation is used for modelling the water while a rigid body model is chosen for the vehicle. The vehicle under consideration is characterized by low weight. This leads to difficulties in modelling the fluid–structure interaction using standard Dirichlet–Neumann coupling. We apply a modified partitioned strategy introducing the interface Laplacian into the pressure Poisson's equation for obtaining a convergent FSI solution. The paper concludes with an industrial example of a vehicle sea-landing modelled using PFEM.



## 1. Introduction and outline

The sea-landing of aerial vehicles is one important practical application where numerical simulation of fluid–structure interaction (FSI) is of great importance since the preliminary physical tests turn out to be excessively expensive. The simulation tests can provide both qualitative and quantitative insight into the movement of the vehicle and predict the impact forces.

It is worth mentioning that up-to-date there exists a rather sparse literature on the sea-landing studies. Experimental investigations of the water landing were presented in Vaughan (1959). Numerical studies can be found e.g. in Littell (2007) where the commercial software LS-DYNA was used. However, several of the existing fluid–structure interaction techniques can be applied to the problem of interest. One such possibility is the Arbitrary Lagrangian Eulerian (ALE) approach known for its accuracy (see e.g. Donea et al., 1982 or Souli et al., 2000). Unfortunately, even the most advanced ALE formulations arrive to their limits when the domain shape deformations are large, which is the case for the problem at hand. In such situations, re-meshing becomes inevitable. Another alternative are the fixed grid approaches equipped with the volume of fluid (VOF) or the Level set method (Legay et al., 2006; Rossi et al., 2013). Although possible, the use of fixed grid methods is not trivial for the problem at hand, since it would require dealing with an FSI boundary cutting the grid elements at arbitrary positions. This would require implementing some sort of embedded technique (Codina et al., 2009; Ryzhakov and Oñate, 2010). Smooth Particle Hydrodynamics (SPH)-based approaches (see e.g. Liu, 2003; Antoci et al., 2007) represent a viable alternative and we verify our formulation against one of the few available benchmark examples (Oger et al., 2006). The problem of the majority of SPH methods is related to the artificial compressibility they usually introduce, which leads to the generation and propagation of non-physical pressure waves in the fluid domain. Such effects may be relevant when estimating the impact forces.

Yet another possibility relies on applying the Particle Finite Element Method (PFEM) (Oñate et al., 2004; Idelsohn et al., 2004; Larese et al., 2008; Ryzhakov et al., 2010). PFEM is a class of Lagrangian Finite Element methods developed for treating free-surface flows and it enables efficient treatment of such complex FSI problems. This option is explored here. We present an approach where the PFEM fluid formulation is coupled to the rigid body model representing the vehicle. The rigid body approximation is a reasonable choice considering that the deformations of the solid are of no interest in the study.

In the present study the unmanned aerial vehicle (UAV) under consideration is characterized by a low weight. The average density, when empty, is some three times lower than that of water. In such case standard Dirichlet–Neumann FSI strategies require excessive number of coupling iterations or do not converge

* Corresponding author. Tel.: +34 934017399.
*E-mail address:* pryzhakov@cimne.upc.edu (P. Ryzhakov).
*URLS:* http://www.cimne.com (P. Ryzhakov), http://www.cimsa.com (A. Viña).

0029-8018/$ - see front matter © 2013 Elsevier Ltd. All rights reserved.
http://dx.doi.org/10.1016/j.oceaneng.2013.03.015

at all. There are several techniques for tackling this problem. Among them there are the under-relaxation techniques (Kuettler and Wall, 2008), Robin–Robin coupling strategies (Badia et al., 2009), methods based on introducing slight compressibility to the fluid (Ryzhakov et al., 2010) and others. We adopt here the FSI coupling equipped with the so-called "interface Laplacian technique" (Idelsohn et al., 2009; Rossi and Oñate, 2010) which ensures convergence. This technique accounts for the structural motion within the pressure Poisson's equation of the fluid. It can be easily implemented within an existing Dirichlet–Neumann coupling.

The paper is organized as follows. First, the basic concepts of the PFEM are introduced. The fractional step technique is applied to solution of the governing system. Next, a rigid body model is described and the FSI coupling scheme is presented. The paper concludes with an example section, where the method is validated first and then applied to a problem of sea-landing of a UAV. Two stages of analysis are presented: the impact of the capsule against water and the floating of the capsule in water.

## 2. The PFEM-based model for the fluid

The PFEM adopts an updated Lagrangian framework for the description of the fluid, where the mesh nodes are treated as particles that can freely move and even separate from the main fluid domain (Oñate et al., 2004; Idelsohn et al., 2004). The key idea of the PFEM is that the variables of interest are stored at the nodes instead of the Gauss points. This results in a hybrid between a standard FE and a mesh-free method. A finite element mesh is created at every time step of the dynamic problem and the solution is then stored at the nodes. The nodes move according to their velocity obtaining their new position and then the finite element mesh is re-generated using a Delaunay triangulation (Delaunay, 1934). In our approach we use simplicial triangular/tetrahedral meshes. In treating problems involving free surface flows the boundary is determined at every time step using the alpha-shape technique (Akkiraju et al., 1995; Oñate et al., 2004).

It is important to remark that the convective term of the momentum equation disappears in the Lagrangian description. Therefore the problem remains elliptic and the discrete system is symmetric. Thus the stability problems faced in Eulerian methods due to the presence of the convective term do not exist in PFEM.

*Governing equations for an incompressible fluid in a Lagrangian framework*: A viscous incompressible flow is described by Navier–Stokes equations, which in the Lagrangian framework can be written as (a Newtonian fluid is considered):

$$\rho\frac{\partial \mathbf{v}}{\partial t}+\nabla p-\nabla\cdot(\mu\nabla\mathbf{v})=\rho\mathbf{g} \tag{1}$$

$$\nabla\cdot\mathbf{v}=0 \tag{2}$$

where $\mathbf{v}$ is the velocity vector, $p$ the pressure, $t$ the time, $\mathbf{g}$ the body force, $\rho$ the density and dynamic viscosity $\mu$.

We define the residual of the momentum and continuity equations as

$$\mathbf{r}_m=\rho\mathbf{g}-\left(\rho\frac{\partial \mathbf{v}}{\partial t}+\nabla p-\nabla\cdot(\mu\nabla\mathbf{v})\right) \tag{3}$$

$$r_c=\nabla\cdot\mathbf{v} \tag{4}$$

The problem to be solved becomes finding $\mathbf{v}$ and $p$ such that

$$\mathbf{r}_m=0 \tag{5}$$

and

$$r_c=0 \tag{6}$$

A discrete version of the governing system obtained using linear equal order velocity–pressure finite elements in space and Backward Euler time integration scheme[1] reads (note that the discrete variables are distinguished from their continuous counterparts by an over-bar)

$$\bar{\mathbf{r}}_m=\bar{\mathbf{F}}^{n+1}-\left(\mathbf{M}\frac{\bar{\mathbf{v}}_{n+1}-\bar{\mathbf{v}}_n}{\Delta t}-\mathbf{G}\bar{\mathbf{p}}_{n+1}+\mu\mathbf{L}\bar{\mathbf{v}}_{n+1}\right)=0 \tag{7}$$

$$\bar{\mathbf{r}}_c=\mathbf{D}\bar{\mathbf{v}}_{n+1}+\mathbf{S}\bar{\mathbf{p}}_{n+1}=0 \tag{8}$$

where $\bar{\mathbf{v}}$ and $\bar{\mathbf{p}}$ are the velocity and pressure respectively, $\bar{\mathbf{F}}$ is the body force vector, $\mathbf{M}$ is the mass matrix, $\mathbf{L}$ is the Laplacian matrix, $\mathbf{G}$ is the gradient matrix and $\mathbf{S}$ is the stabilization matrix necessary for ensuring pressure stability whenever equal order velocity–pressure interpolation is used. Discussing details of the pressure stabilization lie outside of the scope of this work and the ideas presented here can be applied in conjunction with any stabilization technique such as Galerkin/Least squares (GLS) (Hughes et al., 1989), finite calculus (FIC) (Oñate, 2000, 2004), algebraic sub-grid scales (ASGS) or orthogonal sub-scales (OSS) (Codina, 2002). In the present implementation the FIC stabilization method was used.

The matrices are assembled from the elemental contributions defined as

$$\mathbf{M}=\mathbf{M}_{IJIk}=\int_{\Omega_e}\delta_{kl}(N_I,N_J)d\Omega$$

$$\mathbf{L}=\mathbf{L}_{IJ}=\int_{\Omega_e}\left(\frac{\partial N_I}{\partial x_k},\frac{\partial N_J}{\partial x_l}\right)d\Omega$$

$$\mathbf{G}=\mathbf{G}_{IJk}=\int_{\Omega_e}\left(\frac{\partial N_I}{\partial x_k},N_J\right)d\Omega$$

$$\mathbf{D}=\mathbf{G}^T$$

$$\mathbf{F}=\mathbf{F}_{Ik}=\int_{\Omega_e}(N_I,\mathbf{f}_k)\,d\Omega$$

where $N$ stands for the standard linear FE shape functions and $\delta$ is the Kronecker delta function. The capital indices stand for the nodal numbers while lower-case indices refer to the spatial components of a vector.

The fractional step method (Chorin, 1967; Temam, 1969) is applied to the monolithic system defined by Eq. (7) permitting an efficient implementation. It is based on the solution of the momentum equations for an intermediate (non-solenoidal) velocity $\tilde{\mathbf{v}}$ and a subsequent correction performed to obtain the end-of-step velocity $\bar{\mathbf{v}}^{n+1}$. Thus the solution of the governing system equation (7) is replaced by three sequential steps:

$$\tilde{\mathbf{r}}_m=\mathbf{F}_{n+1}-\left(\mathbf{M}\frac{\tilde{\mathbf{v}}-\bar{\mathbf{v}}_n}{\Delta t}-\mathbf{G}\bar{\mathbf{p}}_n+\mu\mathbf{L}\tilde{\mathbf{v}}\right)=0 \tag{9}$$

$$\Delta t\mathbf{L}(\bar{\mathbf{p}}_{n+1}-\bar{\mathbf{p}}_n)+\mathbf{S}\bar{\mathbf{p}}_{n+1}=\mathbf{D}\tilde{\mathbf{v}} \tag{10}$$

$$\mathbf{M}\frac{\bar{\mathbf{v}}_{n+1}-\tilde{\mathbf{v}}}{\Delta t}+\mathbf{G}(\bar{\mathbf{p}}_{n+1}-\bar{\mathbf{p}}_n)=0 \tag{11}$$

Note that the velocity and the pressure solution steps become decoupled. First, Eq. (9) is solved for $\tilde{\mathbf{v}}$ knowing $\bar{\mathbf{p}}_n$ and $\bar{\mathbf{v}}_n$, then the end-of-step pressure $\bar{\mathbf{p}}_{n+1}$ is computed from $\tilde{\mathbf{v}}$ (Eq. (10)). Finally, the end-of-step velocity is found from $\bar{\mathbf{p}}_{n+1}$ and $\tilde{\mathbf{v}}$ according to Eq. (11).

*Re-meshing and boundary definition*: As in the PFEM the mesh is moving in time, the computational mesh undergoes deformation. Therefore, the re-meshing and the re-determination of the domain's boundaries must be executed. In the PFEM the mesh is

[1] The time integration using the Backward Euler scheme is assumed for the sake of simplicity. However, all the arguments presented in the paper can be extended to any implicit time integration scheme.

re-generated at every time step of a dynamic problem using the Delaunay triangulation/tetrahedralization (Delaunay, 1934; Edelsbrunner and Shah, 1996; Calvo and Idelsohn, 2003). When using the term "mesh re-generation" we slightly abuse the terminology since when the Delaunay technique is applied, only the nodal connectivities (and thus elements) change, while the nodes themselves remain generally preserved.

The Delaunay partition facilitates the recognition of the boundary nodes. Considering that the nodes follow a variable $h(x)$ distribution, where $h(x)$ is the minimum distance between two nodes, the following criterion defines the boundary recognition used in the classical PFEM approach (Oñate et al., 2004): all nodes on an empty sphere with a radius greater than $\alpha h$ are considered boundary nodes. In practice $\alpha$ is a parameter close to, but greater than one (typically around 1.5). This criterion is coincident with the "alpha-shape" concept of Edelsbrunner and Shah (1996). As soon as the boundary nodes are identified, the triangles/tetrahedra whose nodes (all nodes) belong to the boundary are erased. The boundary is thus defined by a polygon/polyhedron consisting of segments/faces defined by the boundary nodes.

At this point we described the main ingredients of the PFEM, namely the governing equations in the updated Lagrangian framework, the re-meshing and boundary recognition procedures. Table 1 summarizes the application of PFEM to the solution of a hydrodynamic problem.

Next we describe the rigid body model for the unmanned aerial vehicle (UAV).

## 3. Rigid body model for the UAV

In spacecraft dynamics one commonly stands between two choices: the first consists in developing the equations of motion modelling the spacecraft as a system of point masses (Chobotov, 1991) $m_i$, $i=1,\ldots,n$ resulting $3n$ second order differential equations of motion complemented by $n-1$ distance constraints. Another option, that is widely used in practice consists in modelling the spacecraft as a rigid body. In such case the rotational degrees of freedom need to be taken into account. This leads to some implications related to the choice of the reference frame for formulating the governing equations of motion: Newtons' second law in the body-fixed rotating reference frame has a form different from the habitual (since rotating reference frames are not inertial). However, only six equations describe the motion, as the rigid body is usually represented by its center of mass. The rigid body model is chosen in this work as otherwise different discretizations would require re-computation of mass-point distributions and weights.

*Rigid body governing equation*: The motion of a rigid body can be characterized by six degrees of freedom (translation in three directions and rotation about the three axes). In the following we briefly review the rigid body formulation used in this work.

*Equations of translational motion*: We write the equations of motion in a body-fixed reference frame (which is not inertial). The translational equations of motion are based on the second law of Newton: $\mathbf{f}_{ext}=\partial_t\mathbf{p}$ with the linear momentum of a rigid body defined as $\mathbf{p}=m\mathbf{v}_o$ where $\mathbf{v}_o$ is the velocity of the gravity center of the rigid body.

To use the second law of Newton in a body-fixed rotating reference frame we need to define the map between the kinematic quantities in the inertial and rotating reference frames. Vectors remain invariants, while the relationship between the time derivatives in the inertial and rotating reference frames for a given vector $\mathbf{x}$ reads

$$\left|\frac{d\mathbf{x}}{dt}\right|_i=\left|\frac{d\mathbf{x}}{dt}\right|_b+\omega\times\mathbf{x} \tag{12}$$

Indices "i" and "b" stand for "inertial" and "body" reference frames respectively, $\mathbf{r}$ is the radius vector from the inertial origin to the origin of the rotating reference frame and $\omega$ is the angular velocity of the body-fixed frame with respect to the inertial reference frame (Fig. 1).

The linear momentum of a rigid body in the inertial and body-fixed reference frames is identical as long as the rotating reference frame is located at the gravity center of the rigid body.

Applying Eq. (12) to the linear momentum (assuming that the body-fixed reference frame is located at the gravity center $o$ of the rigid body) and using Newton's second law we obtain the governing equation of translational motion, written for the rotating body-fixed reference frame:

$$\mathbf{f}_{ext}=|\partial_t\mathbf{p}|_i=|\partial_t\mathbf{p}|_o+\boldsymbol{\omega}\times\mathbf{p}=m\partial_t\mathbf{v}_o+\boldsymbol{\omega}\times m\mathbf{v}_o \tag{13}$$

*Rotational equations of a rigid body motion*: Rotational equations of motion for a rigid body can be easily derived from Euler's law, stating that the change of angular momentum around the mass center is equal to the net applied moment about the mass center. We write it first in the classical inertial frame form as

$$\partial_t\mathbf{h}=\mathbf{Q} \tag{14}$$

where $\mathbf{h}$ is the angular momentum about the mass center and $\mathbf{Q}$ is the total applied moment about the mass center.

In the body-fixed reference frame located at the gravity center we can write it as $\mathbf{h}=\mathbf{I}\boldsymbol{\omega}$, where $\mathbf{I}$ is the tensor of second moment of inertia (constant in the body-fixed reference frame, which is one of the reasons why it is convenient to write the equations of motion in the body-fixed frame) and $\boldsymbol{\omega}$ is the angular velocity of the body-fixed reference frame $\mathcal{F}_b$ with respect to the room-fixed frame $\mathcal{F}_i$.

The second moment of inertia $\mathbf{I}$ is defined as

$$\mathbf{I}=\iiint_{\mathcal{B}}(\rho\mathbf{r}^2 I-\mathbf{r}\otimes\mathbf{r})\,dx\,dy\,dz \tag{15}$$

with $I$ being a $3\times3$ identity tensor and $\mathcal{B}$ is the body domain.

In a rotating reference frame $\mathcal{F}_b$ Eq. (14) has the form (we again apply Eq. (12))

$$\partial_t\mathbf{h}+\boldsymbol{\omega}\times\mathbf{h}=\mathbf{Q} \tag{16}$$

Since $\mathbf{h}=\mathbf{I}\boldsymbol{\omega}$ and $\partial_t\mathbf{I}=0$ in the body-fixed frame Eq. (16) yields directly an expression for the angular acceleration:

$$\dot{\boldsymbol{\omega}}=-\mathbf{I}^{-1}\boldsymbol{\omega}\times\mathbf{I}\boldsymbol{\omega}+\mathbf{I}^{-1}\mathbf{Q} \tag{17}$$

If the principal reference frame is used, then the moment of inertia is diagonal and the matrix equation (17) can be expanded to obtain the standard version of Euler's equations for the rotational motion of a rigid body as

$$\dot{\omega}_1=\frac{I_2-I_3}{I_1}\omega_2\omega_3+\frac{Q_1}{I_1} \tag{18}$$

$$\dot{\omega}_2=\frac{I_3-I_1}{I_2}\omega_1\omega_3+\frac{Q_2}{I_2} \tag{19}$$

$$\dot{\omega}_3=\frac{I_1-I_2}{I_3}\omega_1\omega_2+\frac{Q_3}{I_3} \tag{20}$$

**Table 1**
Algorithm for solution of a hydrodynamic problem using PFEM.

1. Discretize the fluid with a finite element mesh
2. Identify the external boundaries for the fluid (using alpha-shape technique)
3. Solve the Lagrangian equations of motion for the fluid (fractional step technique in our case). Compute the relevant state variables: velocities, pressure and displacements
4. Move the mesh nodes to a new position (according to the computed incremental displacement)
5. Re-generate mesh for the fluid domain
6. Go back to the next time step. Start solution from Step 2

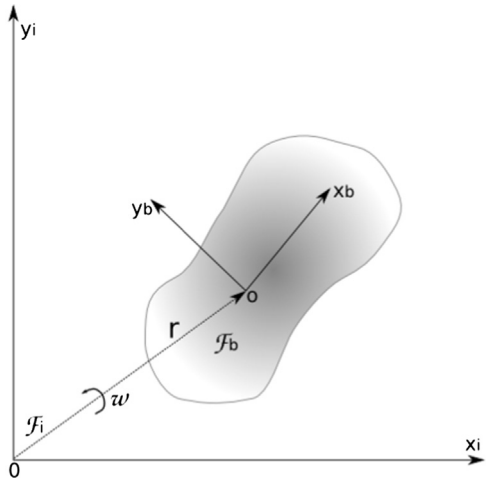


**Fig. 1.** Inertial and body-fixed reference frames.

where indices 1, 2, 3 refer to the directions of the principle axes of rotation.

The set of equations describing the motion of rigid body consists of equations describing translation (Eq. (13)) and three equations for the rotational motion (Eq. (17)). Determination of the primary variables (positions and rotation angles) is obtained by integrating these equations in time. This was done in this work using the same time integration scheme as the ones used for the fluid's equations,which is justified for small time steps. Note that for time integration of the rigid-body equations in the presence of finite rotations there exist specialized quaternion-based schemes (Betsch and Siebert, 2009; Siebert and Betsch, 2008).

*Incremental rotation matrix*: As for now we have defined a set of governing rigid body equations whose solution and integration (in time) shall provide us with the kinematic quantities of the rigid body.

We have decided to write the dynamic equations in the body-fixed reference frame in order not to recompute the moments of inertia. However such choice of reference frame requires transforming the external forces and moments (that are usually given in the room-fixed inertial reference frame) into the rotating body-fixed frame. Thus, a transformation matrix must be defined, mapping a vector or tensor quantity between $\mathcal{F}_b$ and $\mathcal{F}_i$. This necessitates special care: the difficulty arises from the fact that 3D rotations are generally not commutative (Argyris, 1982; Simo and Vu-Quoc, 1986; Ibrahimbegović et al., 1995). The rotation matrix at time $t_n$ is computed as a product of incremental rotation matrices:

$$\mathbf{R}_n^{total} = \mathbf{R}_n^{incr} * \mathbf{R}_{n-1}^{total} = \mathbf{R}_n^{incr} * \mathbf{R}_{n-1}^{incr} * \mathbf{R}_{n-2}^{incr} \dots \mathbf{R}_1^{incr} \tag{21}$$

with the incremental rotation matrix $\mathbf{R}_n^{incr}$ (corresponding to the rotation increments $\delta\theta_x$, $\delta\theta_y$ and $\delta\theta_z$ at time $n$ about the room-fixed axes $x, y$ and $z$) defined as

$$\mathbf{R}_n^{incr} = \begin{pmatrix} c\delta\theta_z c\delta\theta_z + s\delta\theta_z s\delta\theta_x s\delta\theta_y & s\delta\theta_z c\delta\theta_x & -c\delta\theta_z s\delta\theta_y + s\delta\theta_z c\delta\theta_x c\delta\theta_y \\ -s\delta\theta_z c\delta\theta_y + c\delta\theta_z s\delta\theta_x s\delta\theta_y & c\delta\theta_z c\delta\theta_x & s\delta\theta_z s\delta\theta_y + c\delta\theta_z s\delta\theta_x c\delta\theta_y \\ c\delta\theta_x s\delta\theta_y & -s\delta\theta_x & c\delta\theta_x c\delta\theta_y \end{pmatrix} \tag{22}$$

where $s$ and $c$ stand for sinus and cosinus functions respectively.

Using the rotation matrix we can obtain the necessary transformation between $\mathcal{F}_b$ and $\mathcal{F}_i$. Thus a vector $\mathbf{a}$ in the room-fixed reference frame turns into $\mathbf{R}_n^{total}\mathbf{a}$ in the body-fixed reference frame at time $t_n$.

*The skin*: The "skin" of a rigid body in the context of a numerical implementation is a set of the surface nodes resulting from the spatial discretization. Location of a node $A$ of a rigid body is determined by a vector $\mathbf{r}_{A,b}$ in the body fixed reference frame (which does not change). However, the position of a node $A$ in the room-fixed inertial reference frame is $\mathbf{r}_{A,i} = \mathbf{r}_o^i + \mathbf{R}^{total} \cdot \mathbf{r}_{A,b}$ (note that super-indices "i" and "b" are used to distinguish between the reference frames). The first term is the position of body-fixed frame origin usually placed at the mass center of our rigid body. The second term reflects the above-explained rotation transformation.

The computation of the variables at the nodes of the rigid body "skin" is essential for the interaction, as it permits definition of the "external forces" at nodes acting upon the fluid at contact.

## 4. Strongly coupled FSI involving an incompressible fluid and a rigid body

The most standard and straight-forward way of treating FSI problems in partitioned fashion is the Dirichlet–Neumann coupling. This technique relies on independent solution of the fluid and the solid and accounting for the interaction by exchanging the boundary conditions. The fluid sub-problem is supplemented with Dirichlet boundary conditions (ensuring continuity of velocities) and the structural problem takes into account the fluid pressure in the form of Neumann boundary conditions (ensuring continuity of stresses).

Table 2 displays the algorithm for the standard Dirichlet–Neumann FSI coupling in conjunction with the introduced fractional step method:

Generally, Dirichlet–Neumann couplings work well as long as one deals with solids undergoing small deformations and the solid is much heavier than the fluid ($\rho_s/\rho_f \gg 1$). As in our case, the solid has a light weight we must apply additional technique in order to ensure the coupling convergence. For the standard Dirichlet–Neumann technique the convergence problems originate from the computation of fluid pressure (sub-step 4a in Table 2). When computing the fluid pressure according to the pressure Poisson's equation (Eq. (10)) the effect of structural motion upon the fluid is ignored. The idea of improving the Dirichlet–Neumann coupling consists in modifying the second stage of the fractional step scheme (solution of the pressure equation) so as to account for the effect of the velocity of the structure upon the fluid pressure (Idelsohn et al., 2009). The modified equation (10) can be written as (we omit stabilization terms for the sake of simplicity)

$$\mathbf{D}\tilde{\mathbf{v}} = \hat{\mathbf{L}}(\overline{\mathbf{p}}_{n+1} - \overline{\mathbf{p}}_n) \tag{23}$$

where the modified Laplacian is defined as

$$\hat{\mathbf{L}} = \mathbf{L} + \mathbf{L}_I = \mathbf{D}\mathbf{M}^{-1}\mathbf{G} + \mathbf{D}_I\mathbf{M}_I^{-1}\mathbf{G}_I \tag{24}$$

In Eq. (24) $\mathbf{D}_I$, $\mathbf{G}_I$ and $\mathbf{M}_I$ stand for the divergence, gradient and mass matrices respectively corresponding to the fluid–structure interface. For the rigid body the mass matrix is defined by associating to every point of the rigid body skin a fraction of the total mass corresponding to the total number of nodes. Thus, the introduced interface Laplacian $\mathbf{L}_I = \mathbf{D}_I\mathbf{M}_I^{-1}\mathbf{G}_I$ accounts for the effect of the structural motion (inertia) upon the fluid. As the density of the solid (and thus the entries of the mass matrix of the solid) diminishes, its inverse becomes larger and the influence of the interface Laplacian grows.

The introduced modification ensures convergence, while without it the solution is found to be instable. The detailed derivation of the introduced technique on the basis of the original monolithic FSI system as well as additional modifications in the case of flexible structures are given in Rossi et al. (2011) and Idelsohn et al. (2009).

**Table 2**
Standard Dirichlet–Neumann coupling for the FSI with a fractional step.

1. Solve the equations of motion for the structure for displacement $\overline{\mathbf{u}}^0_{n+1}$, using the fluid pressure $\overline{\mathbf{p}}_n$ as an external load
2. Map the displacements to the fluid domain and deform the mesh accordingly
3. Solve fractional momentum equation for $\tilde{\mathbf{v}}$ using $\overline{\mathbf{p}}_n$ Eq. (9).
4. Start loop until convergence in structural displacement
   (a) Solve the fluid pressure equation (second fractional step) for $\overline{\mathbf{p}}^i_{n+1}$ (Eq. (10))
   (b) Solve the structural equations for $\overline{\mathbf{u}}^i_{n+1}$ using $\overline{\mathbf{p}}^i_{n+1}$
   (c) Solve the end-of-step momentum equation for the fluid (last fractional step) (Eq. (11))

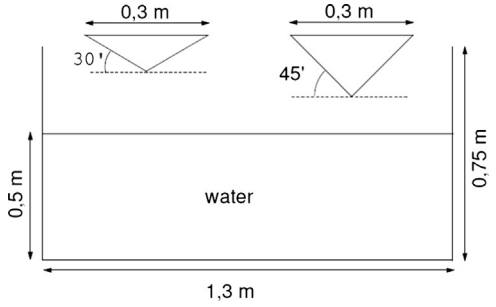


**Fig. 2.** The model: water domain and two configurations of wedges.

## 5. Examples

The solution scheme described in this paper was implemented within the KRATOS Multi-Physics code. KRATOS is a C++ object oriented open source framework developed at CIMNE (Dadvand and Rossi, 2010; Dadvand et al., in press).

### 5.1. Wedge entry

*Free surface evolution*: To evaluate the rigid-body motion coupled with fluid, the analysis of a two-dimensional symmetric wedge entry problems was carried out. The example consists of a solid wedge entering a horizontal bath of water. The calculation is carried out for different dead-rise angles: 30° and 45°. Both wedge configurations are shown in Fig. 2.

The mesh size of 0.5 cm was used for both the wedge and the fluid. The fluid had the standard water properties: dynamic viscosity $\nu = 10^{-3}$ Pa s and density $\rho_f = 1000\ \mathrm{kg/m^3}$). The density of the wedge was set to $\rho_s = 1370\ \mathrm{kg/m^3}$. Zero-velocity boundary condition was applied to the walls of the container. Air was neglected. Initial hydrostatic pressure distribution was prescribed to the fluid.

At $t=0$ s the wedge (its upper edge located 0.25 m above the water surface) starts descending onto the initially still water surface due to gravity. The impact starts at approximately $t=0.18$ s and leads to a large free surface deformation, accompanied by the emergence of two jets running out along the wedge boundaries.

The simulation results are compared with photographs of experiments and numerical results presented in Greenhow and Lin (1983). Fig. 3 shows that numerical results agree well with experimental results for both dead-rise angles. The two jets that appear run out on the boundaries of the wedge and are in good agreement with the experimental studies. The angle at which the jets emerge is also well predicted by our method.

*Acceleration evolution*: Here we continue with the analysis of the wedge impacting the water surface. The geometry is slightly different and the density of the wedge is 1500 kg/m$^3$. The example is taken from Oger et al. (2006), where the temporal evolution of the wedge's acceleration is presented. Air effects are not taken into account. The scheme and the properties are shown in Fig. 4(a).

The computational mesh size of 0.01 m was used for both the wedge and water. A wedge, originally located 0.61 m above the still water surface descends due to gravity. The acceleration in the vertical direction is measured. It is adimensionalized as $\mathbf{a} = \ddot{y}/g$ where $g$ is the gravitational acceleration.

One can see in Fig. 4(b) that the impact takes place at 0.35 s, which is in perfect agreement both with the experimental results and the numerical tests obtained using a Smooth Particle Hydrodynamics (SPH) technique (Oger et al., 2006). The peak acceleration at the moment of impact is approximately 12 adimensional units, which matches well the experimental value and is slightly lower than the one obtained using SPH. Similar to the SPH results, we cannot reproduce the deceleration slope from 0.350 to 0.355 s as the air was not included in the model.

### 5.2. Study of the sea-landing of a UAV

The objective of this work was to model the sea impact of the UAV as well as to analyze the subsequent floating of the capsule. Fig. 5 shows a schematic view of the geometry. The aim of the first phase was to estimate the accelerations due to the impact and to get qualitative insight into the motion of the capsule for different angles of attack. For the analysis of the impact, floats were not considered. The vehicle is designed in a way that the floats get inflated after the impact, i.e. at the moment when danger of sinking appears. The second phase was devoted to the analysis of the forces acting at the security balloons during the floating of the vehicle.

*Properties of the capsule*: For all the analysis cases below the following properties of the vehicle were taken:

- Volume $V = 7.70\ \mathrm{m^3}$.
- Mass $m = 1710$ kg.
- Center of gravity: (1.822,−0.0039,−0.1179).
- Inertia tensor:

$$I = \begin{pmatrix} 492 & 0.0 & 0.0 \\ 0.0 & 2247 & 0.0 \\ 0.0 & 0.0 & 2358 \end{pmatrix}$$

The off-diagonal moments were negligible. The body-fixed reference frame system was located at the center of gravity of the vehicle. The position of the gravity center was counted from the point indicated in Fig. 5, $x$-axis being oriented along the longitudinal axis of the vehicle.

Water was modelled as an incompressible fluid using the PFEM. The fluid domain had a half-cylindrical shape, with length of 10 m in the $x$ direction, and a 180° circular segment cross-section with a radius of 5 m. Water was discretized using 800,000 linear tetrahedral elements.

*Impact simulation*: The first task concerned with the modelling of the impact of the vehicle against the initially still water surface. The capsule was considered impermeable and therefore constant

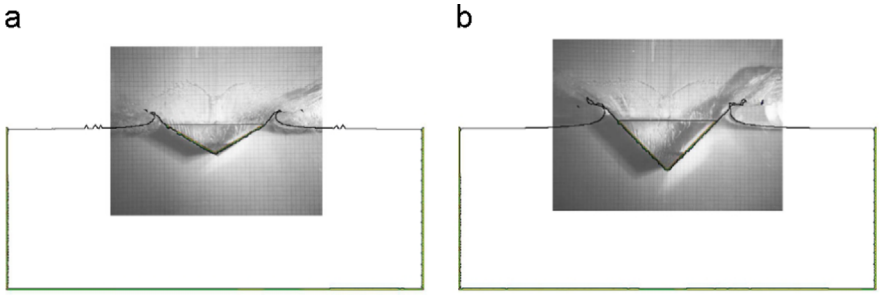


**Fig. 3.** Free surface configuration due to the wedge entry at 0.25 s: comparison with experimental results (superimposed). (a) 30° dead-rise angle. (b) 45° dead-rise angle.

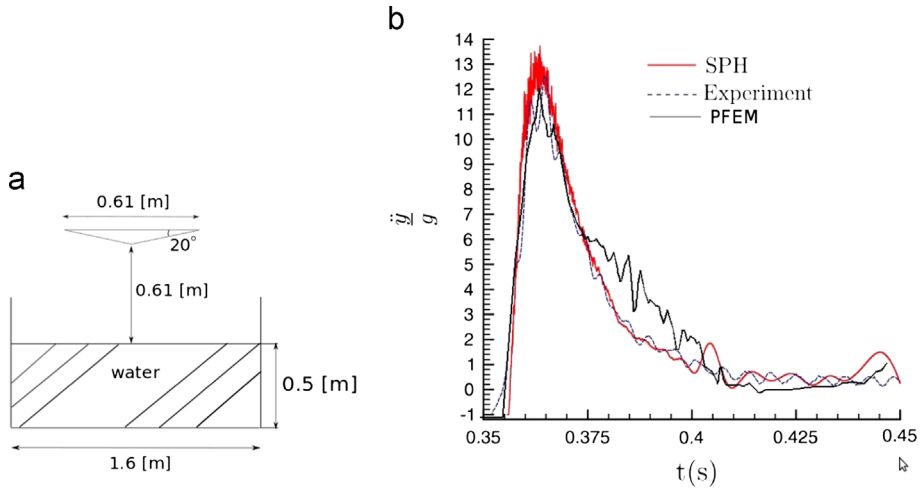


**Fig. 4.** An impact of a wedge with dead-rise angle of 20°. (a) Model. (b) Comparison of the vertical accelerations.

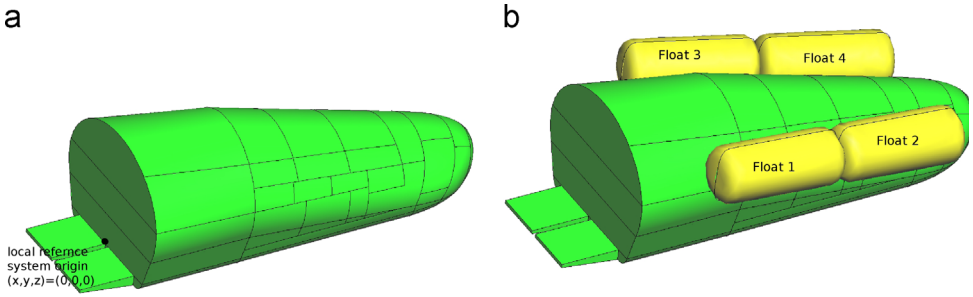


**Fig. 5.** A capsule, floats numbering and origin of the local coordinate system. (a) Capsule. (b) Capsule with floats.

inertia properties were assumed. The main point of interest was the estimation of the maximum accelerations/forces exerted upon the vehicle during the impact as well as the stability of the vehicle (possibility of the flip-over). Several impact scenarios regarding initial velocity and orientation were considered. We reproduce here the results corresponding to the rear and lateral impact corresponding to the angle of attack (i.e. the angle between the longitudinal axis of the vehicle and the water surface) of 19°. This angle of attack was proposed by the industrial partner. In what follows these two cases will be referred to as "rear19" and "lat19", respectively. The initial descent velocities were $v_{x0}=10$ m/s and $v_{z0}=-6$ m/s. At time $t=0.0$ s the capsule was situated at $z_0=3$ m above the water surface. All the results are given in the global (room-fixed) reference frame. A series of snap-shots showing the **rear19** and **lat19** impact scenario is presented in Fig. 6.

*Rear*19: Impact occurs at $t=0.6$ s, that is at the point of time when the horizontal and vertical velocities are $v_x=10$ m/s and vertical velocity $v_y=-10$ m/s, respectively. Fig. 7 depicts velocities and accelerations for the case **Rear19**. The maximum acceleration of the capsule during the impact is reached between 0.5 and 0.6 s and is equal approximately to $7g$, where $g$ is the acceleration due to gravity. In Fig. 7 one can see high frequency fluctuations of the acceleration. We believe that these are non-physical and can be considered "numerical noise".

*Lat*19: In the case of lateral impact flip-over takes place, rendering this case as potentially dangerous. This can be seen in Figs. 6 and 8. One can see that at the end of the simulation ($t\approx3$ s), the capsule turned by 280° around the global vertical axis **z**. This corresponds to 5.5 rad.

The velocity and acceleration evolution is presented in Fig. 9. Impact starts at around 0.6 s, with velocities $v_x\approx10$ m/s, $v_y\approx-10$ m/s. At the moment of impact the velocity component $v_y$ that was initially zero begins to develop and becomes zero again once the flip-over is complete. Maximal vertical acceleration due to impact of ≈80 m/s$^2$ is exhibited at $t=0.65$ s.

The impact accelerations predicted by the present method resulted to match the expected load ranges stated by the industrial partner.

*Floatability analysis*: A floatability analysis of the capsule equipped with inflatable balloons defined the second stage of

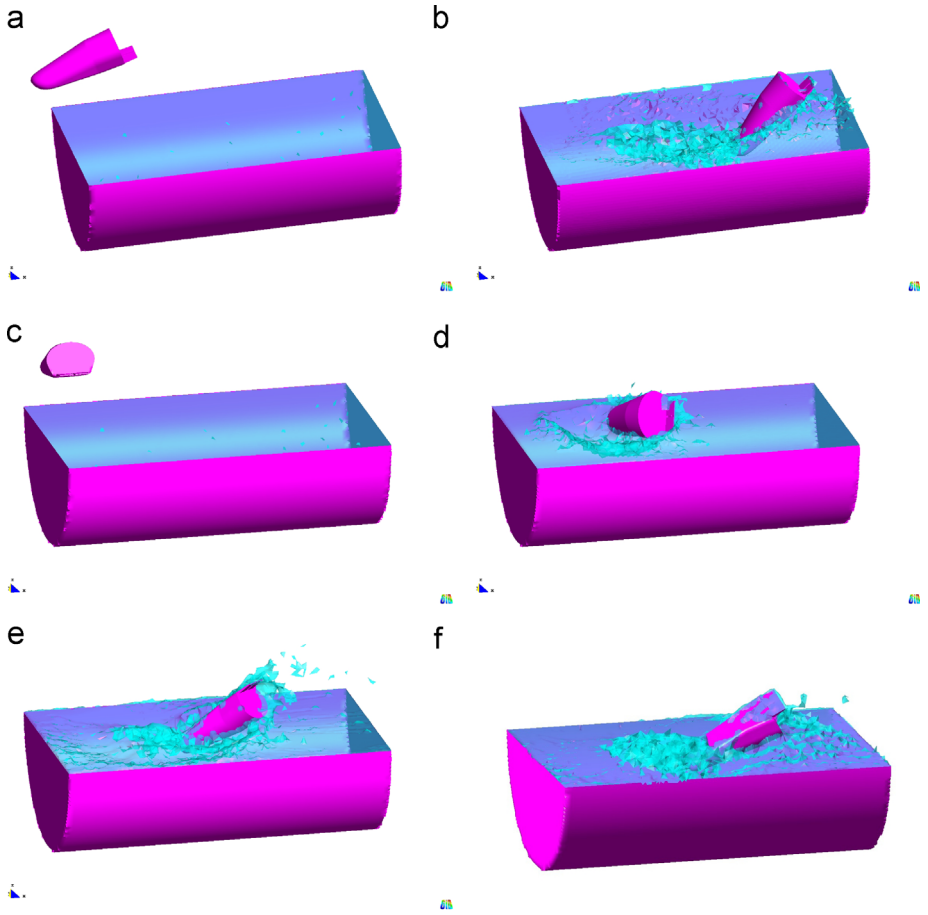


**Fig. 6. Rear** and Lateral impact at two time instances. (a) Rear: 0.0 s. (b) Rear: 1.6 s. (c) Lat: 0 s. (d) Lat: 1 s. (e) Lat: 1.6 s. (f) Lat: 2.0 s.

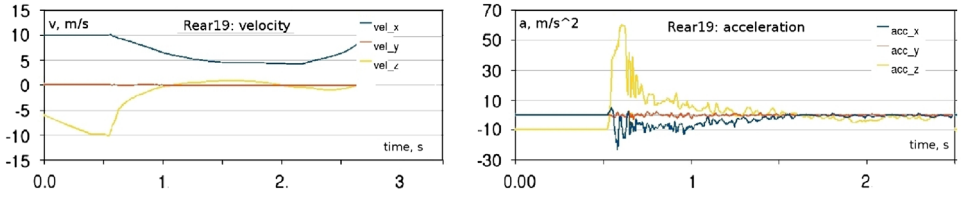


**Fig. 7.** Rear19: velocities and accelerations.

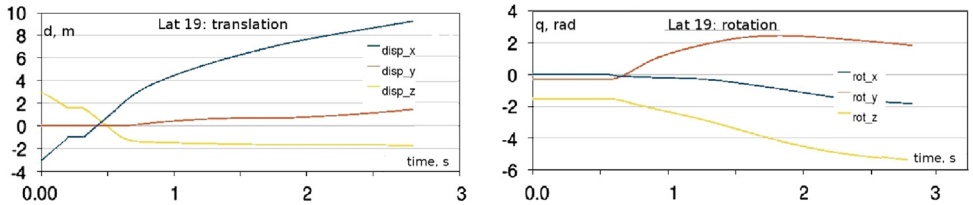


**Fig. 8.** Lateral impact: translations and rotations.

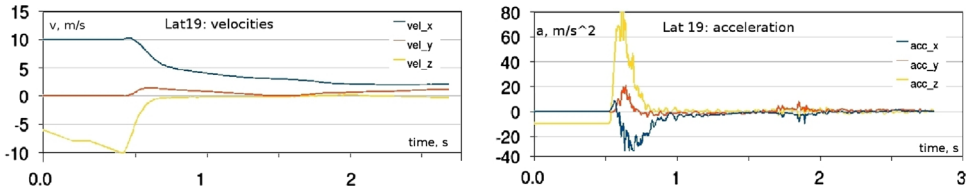


**Fig. 9.** Lateral impact: velocity and acceleration.

analysis. Here, the possibility of water penetration was included. The aim of this analysis was to

1. determine if the volume of the designed floats was sufficient for sustaining the capsule at the water surface;
2. estimate the forces acting upon the floats.

Each float was connected to the capsule at four attachment points modelled as rigid connections. The leakage was not simulated directly, instead, the critical volume of water that can enter into the capsule was estimated and taken into account by appropriate changes of the mass, center of gravity and the moments of inertia of the capsule.

*Scenarios*: The capsule with the floats is initially immersed in water as displayed in Fig. 10.

In order to find the equilibrium position of the capsule in scenarios with water being accumulated at different parts of the capsule, 3 configurations were chosen for the analysis: water accumulated (a) in the front, (b) in the rear, (c) in the lateral part of the capsule. It was assumed that the space between the external panel and internal housing of the capsule is completely filled with water.

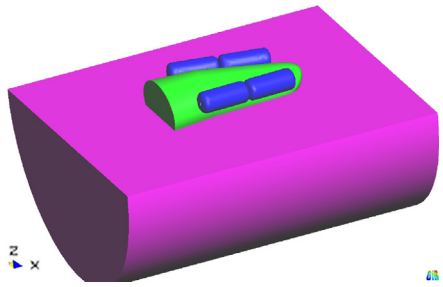

**Fig. 10.** Initial configuration of the capsule for the floatability analysis.

The equilibrium positions obtained in the case of rear and lateral water accumulation are depicted in Fig. 11.

For the sake of brevity we present detailed information of the load evolution for one symmetrical (rear water accumulation) and one non-symmetrical (lateral water accumulation) case only. Fig. 12 represents the temporal evolution of the forces acting on the first and the second floats respectively (due to the symmetry, results for floats N3 and N4 are equivalent to those of N1 and N2 respectively, see Fig. 5).

In the case of accumulation of water at the rear part of the vehicle, only rear floats (N1 and N3) are heavily loaded (see Fig. 12). The maximum force in vertical direction of value $\mathbf{f}_z = 4.2$ kN is exerted upon the rear float at ≈1.5 s. Maximum forces in $x$ and $y$ directions amount to 1.8 kN and 0.5 kN respectively. Forces exerted upon Floats 1 and 3 reach at most 0.5 kN and are negligible.

Fig. 13 represents the temporal evolution acting on the first and the second floats respectively. The floats N3 and N4 in this case undergo much lighter loadings and thus are of no interest in the analysis.

Fig. 13 shows that under the assumption of water accumulation at the side of the vehicle both floats N1 and N2 undergo considerable loading. The maximum force in vertical direction of value $\mathbf{f}_z \approx 5$ kN is exerted upon floats 1 and 2 at ≈1.5 s. Maximal forces in $x$ and $y$ directions amount to 3 kN and 0.5 kN for the rear float (Float1); 3 kN and 1.5 kN for the front float (Float2), respectively. Forces exerted upon Floats 1 and 3 are negligible.

In all the analyzed cases there exist no danger of sinking and no tendency to flip-over was found.

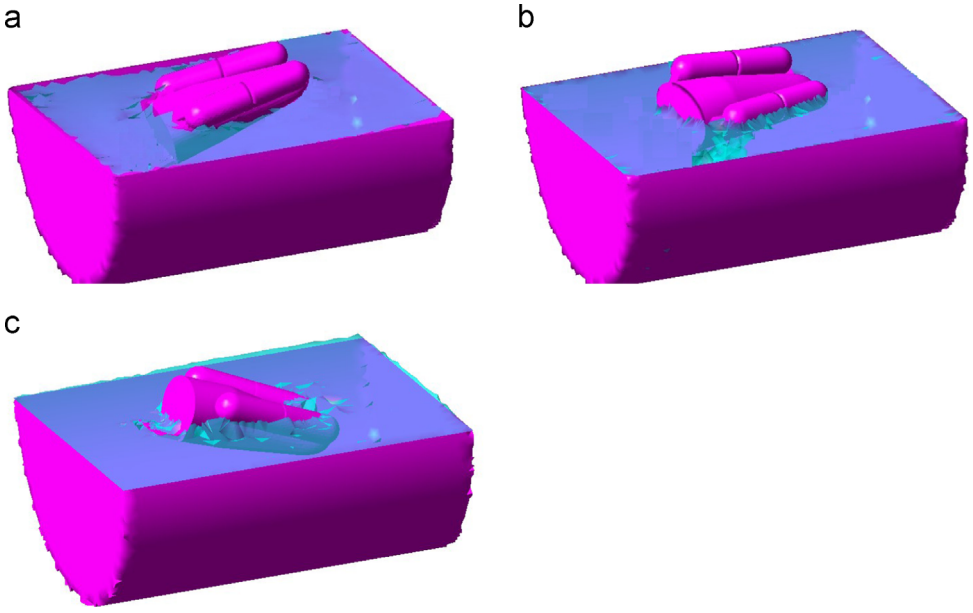


**Fig. 11.** Equilibrium position of the capsule under different water accumulation assumptions. (a) Water accumulated at the rear. (b) Water accumulated at the side. (c) Water accumulated at the front.

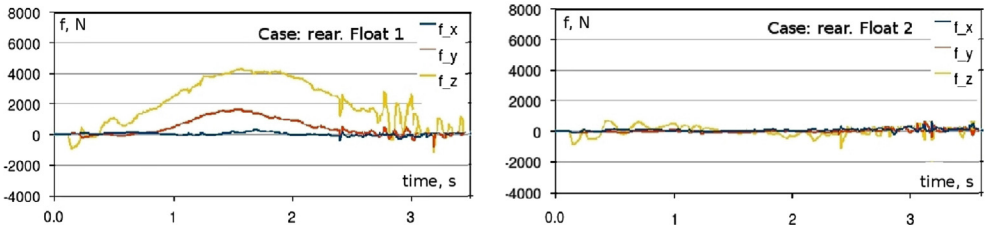


**Fig. 12.** Temporal evolution of forces acting on the floats under assumption of water accumulation at the rear.

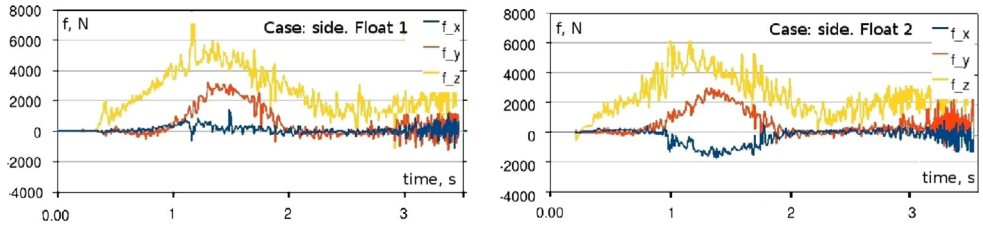


**Fig. 13.** Temporal evolution of forces acting on the floats under assumption of lateral water accumulation.

## 6. Summary and conclusions

In this paper we have developed a formulation for the study of sea-landing of the air vehicles using PFEM. The PFEM and the rigid-body model developed were used in conjunction with a partitioned strategy for the simulation of a challenging industrial FSI problem, namely the sea-landing of a vehicle. The Dirichlet–Neumann coupling strategy was used, enriched by introducing the interface FSI Laplacian accounting for the motion of the structure in calculation of the fluid pressure, and thus capturing the local pressure wave at the fluid–structure interface.

The impact accelerations predicted by the present method are within the expected load ranges stated by the industrial partner. The simulations performed demonstrated that the existing float design ensures that the vehicle remains on the water surface in spite of the water accumulated inside. Depending on water accumulation in the vehicle the maximum load exerted upon the floats were found to be ≈4–6 kN. In either of the three assumptions of water accumulation (front, rear, lateral) only two floats out of 4 actually undergo considerable loading. It was observed in all the simulated cases, that none of them is flip-over prone. That is, the floats assure not only floatability, but also stability of the capsule.

## Acknowledgments

The authors would like to thank *CIMSA Ingenieria y Sistemas* for the financial support of this work.

## References

Akkiraju, N., Edelsbrunner, H., Facello, M., Fu, P., Mucke, E.P., Varela, C., 1995. Alpha shapes: definition and software. In: Proceedings of International Computational Geometry Software Workshop.

Antoci, C., Gallati, M., Sibilla, S., 2007. Numerical simulation of fluid–structure interaction by sph. J. Comput. Struct. 85, 879–890.

Argyris, J., 1982. An excursion into large rotations. Comput. Methods Appl. Mech. Eng. 32, 85–155.

Badia, S., Nobile, F., Vergara, C., 2009. Robin–Robin preconditioned Krylov methods for fluid-structure interaction problems. Comput. Methods Appl. Mech. Eng. 198 (33–36), 2768–2784.

Betsch, P., Siebert, R., 2009. Rigid body dynamics in terms of quaternions: Hamiltonian formulation and conserving numerical integration. Int. J. Numer. Methods Eng. 79 (4), 44–473.

Calvo, N., Idelsohn, S.H., Oñate, E., 2003. The extended Delaunay tessellation. Eng. Comput. 20, 583–600.

Chobotov, V.A., 1991. Spacecraft Attitude Dynamics and Control. Orbit Books edition.

Chorin, A.J., 1967. A numerical method for solving incompressible viscous problems. J. Comput. Phys. 2, 12–26.

Codina, R., 2002. Stabilized finite element approximation of transient incompressible flows using orthogonal subscales. Comput. Methods Appl. Mech. Eng. 191, 4295–4321.

Codina, R., Houzeaux, G., Coppola-Owen, H., Baiges, J., 2009. The fixed-mesh ALE approach for the numerical approximation of flows in moving domains. J. Comput. Phys. Arch. 228, 1591–1611.

Dadvand, P., Rossi, R., Oñate, E., 2010. An object-oriented environment for developing finite element codes for multi-disciplinary applications. Arch. Comput. Methods Eng. 17 (3), 253–297.

Dadvand, P., Rossi, R., Gil, M., Martorell Bofill, X., Juanpere, E., Idelsohn, S., Oñate, E. Migration of a generic multi-physics framework to hpc environments. Comput. Fluids, http://dx.doi.org/10.1016/j.compfluid.2012.02.004, in press.

Delaunay, B., 1934. Sur la sphère vide. Izvestia Akad. Nauk SSSR, Otd. Mat. Estestv. Nauk 7, 793–800.

Donea, J., Giuliani, S., Halleux, J.P., 1982. An arbitrary Lagrangian–Eulerian finite element method for transient dynamic fluid–structure interactions. Comput. Methods Appl. Mech. Eng. 33 (1–3), 689–723.

Edelsbrunner, H., Shah, N., 1996. Incremental topological flipping works for regular triangulations. Algorithmica 15, 223–241.

Greenhow, M., Lin, W.M., 1983. Nonlinear Free Surface Effects: Experiments and Theory. Department of Ocean Engineering Report N. 83-19. MIT.

Hughes, T.J.R., Franca, L.P., Hulbert, G.M., 1989. A new finite element formulation for computational fluid dynamics: VIII. The Galerkin/least-squares method for advective–diffusive equations. Comput. Methods Appl. Mech. Eng. 73 (2), 173–189.

Ibrahimbegović, A., Frey, F., Koz\widehatar, I., 1995. Computational aspects of vector-like parametrization of three-dimensional finite rotations. Int. J. Numer. Methods Eng. 38 (21), 3653–3673.

Idelsohn, S., Oñate, E., Del Pin, F., 2004. The particle finite element method: a powerful tool to solve incompressible flows with free-surfaces and breaking waves. Int. J. Numer. Methods Eng. 61, 964–989.

Idelsohn, S., Del Pin, F., Rossi, R., Oñate, E., 2009. Fluid–structure interaction problems with strong added-mass effect. Int. J. Numer. Methods Eng. 38, 294–309.

Kuettler, U., Wall, W., 2008. Fixed-point fluid–structure interaction solvers with dynamic relaxation. Comput. Mech. 43, 61–72.

Larese, A., Rossi, R., Oñate, E., Idelsohn, S.R., 2008. Validation of the particle finite element method (PFEM) for simulation of free surface flows. Eng. Comput. 25, 385–425.

Legay, A., Chessa, J., Belytschko, T., 2006. An Eulerian–Lagrangian method for fluid–structure interaction based on level-sets. Int. J. Numer. Methods Eng. 195, 2070–2087.

Littell, J.D., 2007. Crew Exploration Vehicle (cev) Water Landing Simulation. Technical Report NASA/TM–2007-214681. NASA.

Liu, G.R., 2003. Smoothed Particle Hydrodynamics, A Meshfree Particle Method. World Scientific Publishing Company edition.

Oger, G., Doring, M., Alessandrini, B., Ferrant, P., 2006. Two-dimensional sph simulations of wedge water entries. J. Comput. Phys. 213 (2), 803–822.

Oñate, E., 2000. A stabilized finite element method for incompressible viscous flows using a finite increment calculus formulation. Comput. Methods Appl. Mech. Eng. 182, 355–370.

Oñate, E., 2004. Possibilities of finite calculus in computational mechanics. Int. J. Numer. Methods Eng. 60 (1), 255–281.

Oñate, E., Idelsohn, S., Del Pin, F., Aubry, R., 2004. The particle finite element method: an overview. Int. J. Comput. Methods 1, 267–307.

Rossi, R., Oñate, E., 2010. Analysis of some partitioned algorithms for fluid–structure interaction. Eng. Comput. 27 (1), 22–56.

Rossi, R., Idelsohn, S., Oñate, E., Cotela, J., Del Pin, F., 2011. Mejora de la solucin fuertemente acoplada de problemas fsi mediante una aproximación de la matriz tangente de presion. Rev. Int. Metodos Numericos para Calculo y Diseño en Ing. 27 (3), 165–179.

Rossi, R., Larese, A., Dadvand, P., Oate, E., 2013. An efficient edge-based level set finite element method for free surface flow problems. Int. J. Numer. Methods Fluids 71 (6), 687–716.

Ryzhakov, P., Oñate, E., Rossi, R., Idelsohn. 2010. Lagrangian FE Methods for Coupled Problems in Fluid Mechanics. CIMNE edition.

Ryzhakov, P., Rossi, R., Idelsohn, S., Oñate, E., 2010. A monolithic Lagrangian approach for fluid–structure interaction problems. J. Comput. Mech. 46 (6), 399–883.

Siebert, B., Betsch, P., 2008. Numerical integration of rigid body dynamics in terms of quaternions. Proc. Appl. Math. Mech. 8 (1), 10139–10140.

Simo, J.C., Vu-Quoc, L., 1986. On the dynamics of flexible beams under large overall motions—the plane case. Appl. Mech. ASME 53, 849–863.

Souli, M., Ouahsine, A., Lewin, L., 2000. Ale formulation for fluid–structure interaction problems. Comput. Methods Appl. Mech. Eng. 190 (5–7), 659–675.

Temam, R., 1969. Sur lapproximation de la solution des equations de Navier–Stokes par la methode des pase fractionaires. Arch. Ration. Mech. Anal. 32, 135–153.

Vaughan, V.L., 1959. Water-landing Impact Accelerations for Three Models of Reentry Capsules. Technical Report D-145. NASA.